



HAL
open science

Surface plasmon polariton beams from an electrically excited plasmonic crystal

Damien Canneson, Eric Le Moal, Shuiyan Cao, Xavier Quélin, Herve Dallaporta, Gérald Dujardin, Elizabeth Boer-Duchemin

► **To cite this version:**

Damien Canneson, Eric Le Moal, Shuiyan Cao, Xavier Quélin, Herve Dallaporta, et al.. Surface plasmon polariton beams from an electrically excited plasmonic crystal. *Optics Express*, 2016, 24 (23), pp.26186-26200. 10.1364/OE.24.026186 . hal-01454995

HAL Id: hal-01454995

<https://hal.science/hal-01454995>

Submitted on 16 Dec 2022

HAL is a multi-disciplinary open access archive for the deposit and dissemination of scientific research documents, whether they are published or not. The documents may come from teaching and research institutions in France or abroad, or from public or private research centers.

L'archive ouverte pluridisciplinaire **HAL**, est destinée au dépôt et à la diffusion de documents scientifiques de niveau recherche, publiés ou non, émanant des établissements d'enseignement et de recherche français ou étrangers, des laboratoires publics ou privés.



Distributed under a Creative Commons Attribution 4.0 International License

Surface plasmon polariton beams from an electrically excited plasmonic crystal

DAMIEN CANNESON,¹ ERIC LE MOAL,^{1,*} SHUIYAN CAO,¹ XAVIER QUÉLIN,² HERVÉ DALLAPORTA,³ GÉRALD DUJARDIN,¹ AND ELIZABETH BOER-DUCHEMIN¹

¹*Institut des Sciences Moléculaires d'Orsay (ISMO), CNRS, Univ Paris Sud, Université Paris-Saclay, 91405 Orsay, France*

²*Groupe d'Étude de la Matière Condensée (GEMaC), UMR 8635 CNRS, UVSQ, Université Paris-Saclay, 45 avenue des Etats-Unis, 78035 Versailles, France*

³*Aix Marseille Université, CNRS, CINaM UMR 7325, 13288 Marseille, France*

*eric.le-moal@u-psud.fr

<http://www.nanosciences.ismo.u-psud.fr>

Abstract: Surface plasmon polariton (SPP) beams with an in-plane angular spread of 8° are produced by electrically exciting a 2D plasmonic crystal using a scanning tunneling microscope (STM). The plasmonic crystal consists of a gold nanoparticle (NP) array on a thin gold film on a glass substrate and it is the inelastic tunnel electrons (IET) from the STM that provide a localized and spectrally broadband SPP source. Surface waves on the gold film are shown to be essential for the coupling of the local, electrical excitation to the extended NP array, thus leading to the creation of SPP beams. A simple model of the scattering of SPPs by the array is used to explain the origin and direction of the generated SPP beams under certain conditions. In order to take into account the broadband spectrum of the source, calculations realized using finite-difference time-domain (FDTD) methods are obtained, showing that bandgaps for SPP propagation exist for certain wavelengths and indicating how changing the pitch of the NP array may enhance the SPP beaming effect.

© 2016 Optical Society of America

OCIS codes: (240.6680) Surface plasmons; (250.5403) Plasmonics; (240.7040) Tunneling; (350.4238) Nanophotonics and photonic crystals.

References and links

1. E. Yablonovitch, "Inhibited spontaneous emission in solid-state physics and electronics," *Phys. Rev. Lett.* **58**, 2059–2062 (1987).
2. T. F. Krauss, R. M. De La Rue, and S. Brand, "Two-dimensional photonic-bandgap structures operating at near-infrared wavelengths," *Nature* **383**, 699–702 (1996).
3. S. Noda, K. Tomoda, N. Yamamoto, and A. Chutinan, "Full three-dimensional photonic bandgap crystals at near-infrared wavelengths," *Science* **289**, 604–606 (2000).
4. Y. Akahane, T. Asano, B.-S. Song, and S. Noda, "High-Q photonic nanocavity in a two-dimensional photonic crystal," *Nature* **425**, 944–947 (2003).
5. W. L. Barnes, T. W. Preist, S. C. Kitson, J. R. Sambles, N. P. K. Cotter, and D. J. Nash, "Photonic gaps in the dispersion of surface plasmons on gratings," *Phys. Rev. B* **51**, 11164–11167 (1995).
6. S. C. Kitson, W. L. Barnes, and J. R. Sambles, "Full photonic band gap for surface modes in the visible," *Phys. Rev. Lett.* **77**, 2670–2673 (1996).
7. S. C. Kitson, W. L. Barnes, and J. R. Sambles, "Surface-plasmon energy gaps and photoluminescence," *Phys. Rev. B* **52**, 11441–11445 (1995).
8. E. Devaux, T. W. Ebbesen, J.-C. Weeber, and A. Dereux, "Launching and decoupling surface plasmons via micro-gratings," *Appl. Phys. Lett.* **83**, 4936–4938 (2003).
9. A. Drezet, A. Hohenau, A. L. Stepanov, H. Ditlbacher, B. Steinberger, F. R. Aussenegg, A. Leitner, and J. R. Krenn, "Surface plasmon polariton Mach-Zehnder interferometer and oscillation fringes," *Plasmonics* **1**, 141–145 (2006).
10. A. Drezet, D. Koller, A. Hohenau, A. Leitner, F. R. Aussenegg, and J. R. Krenn, "Plasmonic crystal demultiplexer and multiplexers," *Nano Lett.* **7**, 1697–1700 (2007).
11. R. Zia, J. A. Schuller, A. Chandran, and M. L. Brongersma, "Plasmonics: the next chip-scale technology," *Mater. Today* **9**, 20–27 (2006).
12. A. Babuty, A. Bousseksou, J.-P. Tetienne, I. M. Doyen, C. Sirtori, G. Beaudoin, I. Sagnes, Y. De Wilde, and R. Colombelli, "Semiconductor surface plasmon sources," *Phys. Rev. Lett.* **104**, 226806 (2010).

13. R. F. Service, "Ever-smaller lasers pave the way for data highways made of light," *Science* **328**, 810–811 (2010).
14. D. W. Pohl, S. G. Rodrigo, and L. Novotny, "Stacked optical antennas," *Appl. Phys. Lett.* **98**, 023111 (2011).
15. P. Rai, N. Hartmann, J. Berthelot, J. Arocas, G. Colas des Francs, A. Hartschuh, and A. Bouhelier, "Electrical excitation of surface plasmons by an individual carbon nanotube transistor," *Phys. Rev. Lett.* **111**, 026804 (2013).
16. K. Ding and C. Z. Ning, "Fabrication challenges of electrical injection metallic cavity semiconductor nanolasers," *Semicond. Sci. Tech.* **28**, 124002 (2013).
17. K. C. Y. Huang, M.-K. Seo, T. Sarmiento, Y. Huo, J. S. Harris, and M. L. Brongersma, "Electrically driven subwavelength optical nanocircuits," *Nat. Photonics* **8**, 244–249 (2014).
18. M. Parzefall, P. Bharadwaj, A. Jain, T. Taniguchi, K. Watanabe, and L. Novotny, "Antenna-coupled photon emission from hexagonal boron nitride tunnel junctions," *Nat. Nanotechnol.* **10**, 1058–1063 (2015).
19. J. Kern, R. Kullock, J. Prangma, M. Emmerling, M. Kamp, and B. Hecht, "Electrically driven optical antennas," *Nat. Photonics* **9**, 582–586 (2015).
20. Y. Vardi, E. Cohen-Hoshen, G. Shalem, and I. Bar-Joseph, "Fano resonance in an electrically driven plasmonic device," *Nano Lett.* **16**, 748–752 (2016).
21. N. Cazier, M. Buret, A. V. Uskov, L. Markey, J. Arocas, G. Colas Des Francs, and A. Bouhelier, "Electrical excitation of waveguided surface plasmons by a light-emitting tunneling optical gap antenna," *Opt. Express* **24**, 3873–3884 (2016).
22. W. Du, T. Wang, H.-S. Chu, L. Wu, R. Liu, S. Sun, W. K. Phua, L. Wang, N. Tomczak, C. A. Nijhuis, "On-chip molecular electronic plasmon sources based on self-assembled monolayer tunnel junctions," *Nat. Photonics* **10**, 274–281 (2016).
23. T. Wang, C. A. Nijhuis, "Molecular electronic plasmonics," *Appl. Mater. Today* **3**, 73–86 (2016).
24. K. Takeuchi and N. Yamamoto, "Visualization of surface plasmon polariton waves in two-dimensional plasmonic crystal by cathodoluminescence," *Opt. Express* **19**, 12365–12374 (2011).
25. H. Watanabe, M. Honda, and N. Yamamoto, "Size dependence of band-gaps in a one-dimensional plasmonic crystal," *Opt. Express* **22**, 5155–5165 (2014).
26. H. Saito, S. Mizuma, and N. Yamamoto, "Confinement of surface plasmon polaritons by heterostructures of plasmonic crystals," *Nano Lett.* **15**, 6789–6793 (2015).
27. B. Stein, J.-Y. Laluet, E. Devaux, C. Genet, and T. W. Ebbesen, "Surface plasmon mode steering and negative refraction," *Phys. Rev. Lett.* **105**, 266804 (2010).
28. B. Stein, E. Devaux, C. Genet, and T. W. Ebbesen, "Self-collimation of surface plasmon beams," *Opt. Lett.* **37**, 1916–1918 (2012).
29. R. Berndt, J. K. Gimzewski, and P. Johansson, "Inelastic tunneling excitation of tip-induced plasmon modes on noble-metal surfaces," *Phys. Rev. Lett.* **67**, 3796 (1991).
30. P. Johansson, "Light emission from a scanning tunneling microscope: fully retarded calculation," *Phys. Rev. B* **58**, 10823 (1998).
31. T. Wang, E. Boer-Duchemin, Y. Zhang, G. Comtet, and G. Dujardin, "Excitation of propagating surface plasmons with a scanning tunnelling microscope," *Nanotechnology* **22**, 175201 (2011).
32. T. Wang, G. Comtet, E. Le Moal, G. Dujardin, A. Drezet, S. Huant, and E. Boer-Duchemin, "Temporal coherence of propagating surface plasmons," *Opt. Lett.* **39**, 6679 (2014).
33. A. Drezet, A. Hohenau, D. Koller, A. Stepanov, H. Dittlacher, B. Steinberger, F. R. Aussenegg, A. Leitner, and J. R. Krenn, "Leakage radiation microscopy of surface plasmon polaritons," *Mater. Sci. Eng. B Adv.* **149**, 220–229 (2008).
34. A. G. Nikitin, A. V. Kabashin, and H. Dallaporta, "Plasmonic resonances in diffractive arrays of gold nanoantennas: near and far field effects," *Opt. Express* **20**, 27941–27952 (2012).
35. A. G. Nikitin, T. Nguyen, and H. Dallaporta, "Narrow plasmon resonances in diffractive arrays of gold nanoparticles in asymmetric environment: experimental studies," *Appl. Phys. Lett.* **102**, 221116 (2013).
36. W. M. Haynes, *CRC Handbook of Chemistry and Physics*, 96th ed. (CRC, 2015).
37. E. Le Moal, S. Marguet, B. Rogez, S. Mukherjee, P. Dos Santos, E. Boer-Duchemin, G. Comtet, and G. Dujardin, "An electrically excited nanoscale light source with active angular control of the emitted light," *Nano Lett.* **13**, 4198–4205 (2013).
38. E. Le Moal, S. Marguet, D. Cannesson, B. Rogez, E. Boer-Duchemin, G. Dujardin, T. V. Teperik, D.-C. Marinica, and A. G. Borisov, "Engineering the emission of light from a scanning tunneling microscope using the plasmonic modes of a nanoparticle," *Phys. Rev. B* **93**, 035418 (2016).
39. P. J. Compaijen, V.A. Malshev, and J. Knoester, "Surface-mediated light transmission in metal nanoparticle chains," *Phys. Rev. B* **87**, 205437 (2013).
40. T. Wang, B. Rogez, G. Comtet, E. Le Moal, W. Abidi, H. Remita, G. Dujardin, E. Boer-Duchemin, "Scattering of electrically excited surface plasmon polaritons by gold nanoparticles studied by optical interferometry with a scanning tunneling microscope," *Phys. Rev. B* **92**, 045438 (2015).
41. J. Wang, C. Zhao, and J. Zhang, "Does the leakage radiation profile mirror the intensity profile of surface plasmon polaritons?," *Opt. Lett.* **35**, 1944–1946 (2010).
42. A. Drezet and C. Genet, "Imaging surface plasmons: from leaky waves to far-field radiation," *Phys. Rev. Lett.* **110**, 213901 (2013).
43. N. W. Ashcroft and N. D. Mermin, *Solid State Physics* (Holt, Rinehart and Winston, 1976).
44. L. Novotny and B. Hecht, *Principles of Nano-Optics* (Cambridge University, 2006).

45. D. Hone, B. Mühlischlegel, and D. J. Scalapino, "Theory of light emission from small particle tunnel junctions," *Appl. Phys. Lett.* **33**, 203 (1978).
46. F. Bigourdan, J.-P. Hugonin, F. Marquier, C. Sauvan, and J.-J. Greffet, "Nanoantenna for electrical generation of surface plasmon polaritons," *Phys. Rev. Lett.* **116**, 106803 (2016).

1. Introduction

Wave propagation in a material may be dramatically modified by periodic structuring on the scale of wavelength. In such materials, Bragg reflections from lattice planes may interfere with the incident waves, thus changing the dispersion relation of the medium and making it very anisotropic. Gaps may occur in the energy-momentum dispersion relation and as a result, wave propagation at specific frequencies and in specific directions may be forbidden [1]. This is the principle of photonic crystals [2], which are artificial dielectric materials having optical properties tailored for applications, such as the fabrication of miniaturized waveguides and lasing resonant cavities [3,4]. A similar approach, referred to as *plasmonic crystals*, has been developed to control the propagation of *surface plasmon polaritons* (SPPs), i.e., electromagnetic waves bound to collective oscillations of electrons at the surface of a metal [5]. Plasmonic crystals often consist of periodic arrays of nanoholes or nanodots on a continuous metallic film. For instance, it has been reported that SPP propagation on a silver film can be blocked in all directions of the plane for a given energy range when its surface is textured with an hexagonal array of nanodots [6]. This effect, which is due to the existence of energy gaps, has been used to inhibit the spontaneous emission of quantum emitters close to metallic surfaces [7]. There is also increasing interest in plasmonic crystals for the fabrication of diffractive optical microelements for plasmonic circuitry [8–10].

Recently, there has been a rapidly growing trend in plasmonics toward the development of nano- and microdevices that are electrically driven with low-energy electrons in the view of integration with nanoelectronics [11–23]. This trend has yielded some very exciting achievements such as electrical nanosources of light and SPPs based on nanoscale light emitting devices (LED) [17] or tunnel junctions [19–22]. Yet, the coupling of such electrical light and SPP nanosources to a plasmonic crystal has never been envisaged so far. Most often, plasmonic crystals are excited using a laser or, more rarely, high-energy electrons in the vacuum of an electron microscope [24–26]; however, local, low-energy, electrical excitation under ambient conditions is preferable for applications in electronics. Another crucial requirement for future applications in plasmonic circuitry is the capacity to steer SPP *beams*, i.e., to concentrate the energy emitted by the SPP nanosource in specific directions. SPP steering and auto-collimation have been observed in 1D and 2D sinusoidal metallic gratings when the SPP wavelength matches the diagonal of the lattice unit cell [27, 28]. Until now, however, such studies have been limited to the optical excitation of SPPs with a laser beam.

In this paper, we electrically excite SPPs in a plasmonic crystal and produce SPP beams in particular directions. The plasmonic crystal consists of a gold nanoparticle (NP) array supported by a thin gold film on a glass substrate. Low-energy electrical excitation is achieved using the inelastic tunnel electrons (IET) from the tip of a scanning tunneling microscope (STM). Such an excitation method is extremely local and the power spectrum of the resulting emission is broad [29–32]. Both localized surface plasmons (LSPs) and propagating SPPs on the gold film may be excited in this way. We collect the light emitted by the surface plasmons in the substrate using the objective lens of an optical microscope, and analyze the results in both the real and Fourier spaces [31]. SPP leakage radiation [33] reveals the spatial distribution and propagation directions of SPPs on the gold film, both inside and outside the NP array. The experimental results are compared to finite-difference time-domain (FDTD) calculations and a simple dipole model. The effects of the substrate, array geometry and source location on the resulting emission are studied. In this way we determine how SPPs mediate the coupling of a local, low-energy,

electrical excitation to the extended modes of a plasmonic nanostructure array.

2. Methods

2.1. Experimental setup

Figure 1(a) shows the experimental setup used in this work. The apparatus consists of a commercial STM head coupled to an inverted optical microscope that is equipped with an oil-immersion, high numerical aperture ($NA = 1.49$), $100\times$ objective lens. During experiments, the STM tip is grounded and the sample is biased to $U_b = 2.8$ V. When the tip is located on a gold NP of the array, IET and the resulting excitation of surface plasmons in the sample yield light in the substrate which is collected with the objective lens. The *spatial* and *angular* distributions of the collected light are thus measured in this way by *real-space* and *Fourier-space* imaging respectively on a water-cooled CCD camera. In Fourier-space imaging, the *back focal plane* of the objective is imaged on the CCD. Note that the emitted light is spectrally broad, with an upper bound to the photon energy given by the energy of the tunnel electrons (i.e., photon energy $h\nu \leq e|U_b|$ where $-e$ is the electric charge of the electron) and extending to the infrared. Note also that the STM tips are fabricated from a tungsten wire that is electrochemically etched in a sodium hydroxide solution (radius of curvature at the tip apex is typically 30 nm).

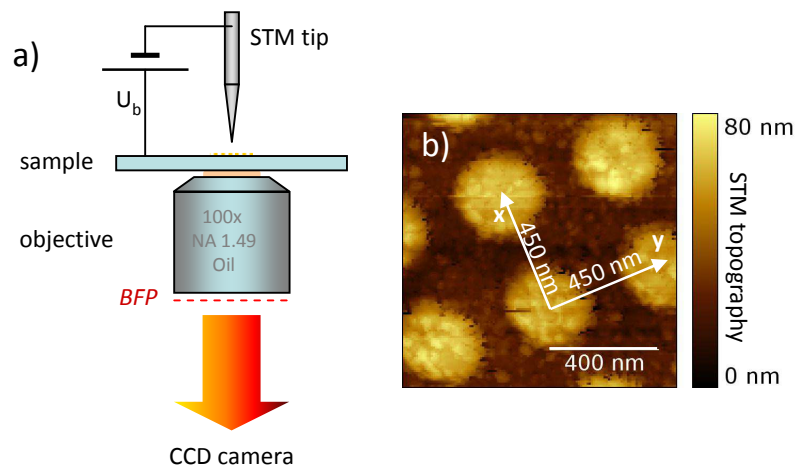


Fig. 1. Experimental setup and the geometry of a gold NP array. (a) Local electrical excitation of the sample is carried out using inelastic electron tunneling from the tip of an STM. The resulting light for real-space and Fourier-space imaging is collected and recorded on a CCD camera. *BFP* represents the back focal plane of the objective lens. (b) $1 \times 1 \mu\text{m}^2$ STM topography image of the gold NP array on a gold film that has a square $450 \times 450 \text{ nm}^2$ unit cell. NPs are 170 nm in diameter and 50 nm high. The apparent width of the NPs in the image is increased due to the convolution with the STM tip (radius of curvature $\approx 50 - 100$ nm).

2.2. Sample fabrication

Periodic gold NP arrays are fabricated by e-beam lithography on glass coverslips coated with either a thermally evaporated 50-nm gold layer or a 100-nm indium tin oxide (ITO) layer. Gold NPs are arranged in periodic arrays of 40×40 NPs with either a square $450 \times 450 \text{ nm}^2$ unit cell or a rectangular $330 \times 550 \text{ nm}^2$ unit cell. An STM topography image of the square array is shown in Fig. 1(b). The shape of the gold NPs is a disc that has a 170 nm diameter and is 50 nm

high. Recently, collective effects have been both theoretically and experimentally demonstrated in the optical extinction spectra of these gold NP arrays on ITO [34, 35].

2.3. Calculations

3D Finite Difference Time Domain (FDTD) calculations are carried out using the commercial software FDTD Solutions from Lumerical. A gold NP array is modeled as a regular 41×41 array of discs, 170 nm in diameter and 50 nm high, with a square $450 \times 450 \text{ nm}^2$ unit cell or a rectangular $330 \times 550 \text{ nm}^2$ unit cell, on an ITO or gold film on a glass substrate. An odd number of gold NPs (i.e., 41 NPs rather than 40) along each line and row is considered for symmetry reasons; thus, the problem has a four-fold rotational symmetry with respect to the vertical axis when the excitation source is located on the central NP of the array. The dielectric function of gold that is used is from Ref. [36]. IET in the tip-sample junction is modeled as a point-like, vertical, monochromatic, electric dipole (along the z axis) located on top of (i.e., in air) and centered on a gold NP; the presence of the tip is ignored. Simulations are performed at various oscillation frequencies of this monochromatic excitation source, varying in vacuum wavelength from $\lambda_0 = 600 \text{ nm}$ to 900 nm in steps of 10 nm , and the results are incoherently summed with weighting factors obtained from experimentally measured spectra. This is an empirical method of taking into account the IET power distribution and the detection efficiency of our setup. Along the x and y directions, the calculation box extends a few microns beyond the boundaries of the NP arrays, in order to examine SPP propagation outside the array and to let SPPs sufficiently decay before meeting Perfectly Matched Layers (PML), thus limiting parasitic reflections. The electric field distribution is calculated in a plane just above the gold NP array (i.e., in air).

A simple 2D, scalar dipole model is also used. Here, a gold NP array is modeled as a group of point-like, vertical, monochromatic, electric dipoles in the horizontal plane. The dipoles are located at the nodes of a periodic 41×41 mesh (array periods are the same as those considered in the FDTD calculations). The amplitude and phase of the dipole oscillations are defined with respect to their distance from the excitation source and weighted by an effective polarizability (with the exception of the dipole at the center of the array which models the excitation source). The distance dependence is given by the SPP propagation length on the gold film or by the decay of the dipole free-space radiation in air, while the effective polarizability takes into account the (in-plane) SPP-to-SPP scattering efficiency of the gold NPs. For simplicity, this weighting factor is the same for all NPs and is set to 0.2 in order to best fit the experimental images. Simulations are conducted for dipole oscillation frequencies corresponding to λ_0 ranging from 600 nm to 900 nm in steps of 10 nm and then incoherently summed with the same weighting factors taken from experimental spectra as for the FDTD calculations.

3. Results and discussion

Figure 2 shows the real-space images recorded upon electrical excitation of the square gold NP array on ITO, the square gold NP array on gold and the *rectangular* gold NP array on gold. From such images we determine the spatial distribution of the resulting light and examine the effect of the substrate and array geometry. In order to obtain these results, the STM excitation is located in the center of the array or, more precisely, on one of the four equivalent particles closest to the array center (due to the even number of particles in the square array, no particle exists in the geometrical center of the array). In practice, we first identify the lateral position of the tip by optical microscopy and then use an STM topography image similar to the one shown in Fig. 1(b) to finely adjust the tip position on the center of a gold NP. In this way the inelastic tunnel current excites the vertical localized surface plasmon mode of the NP [37, 38].

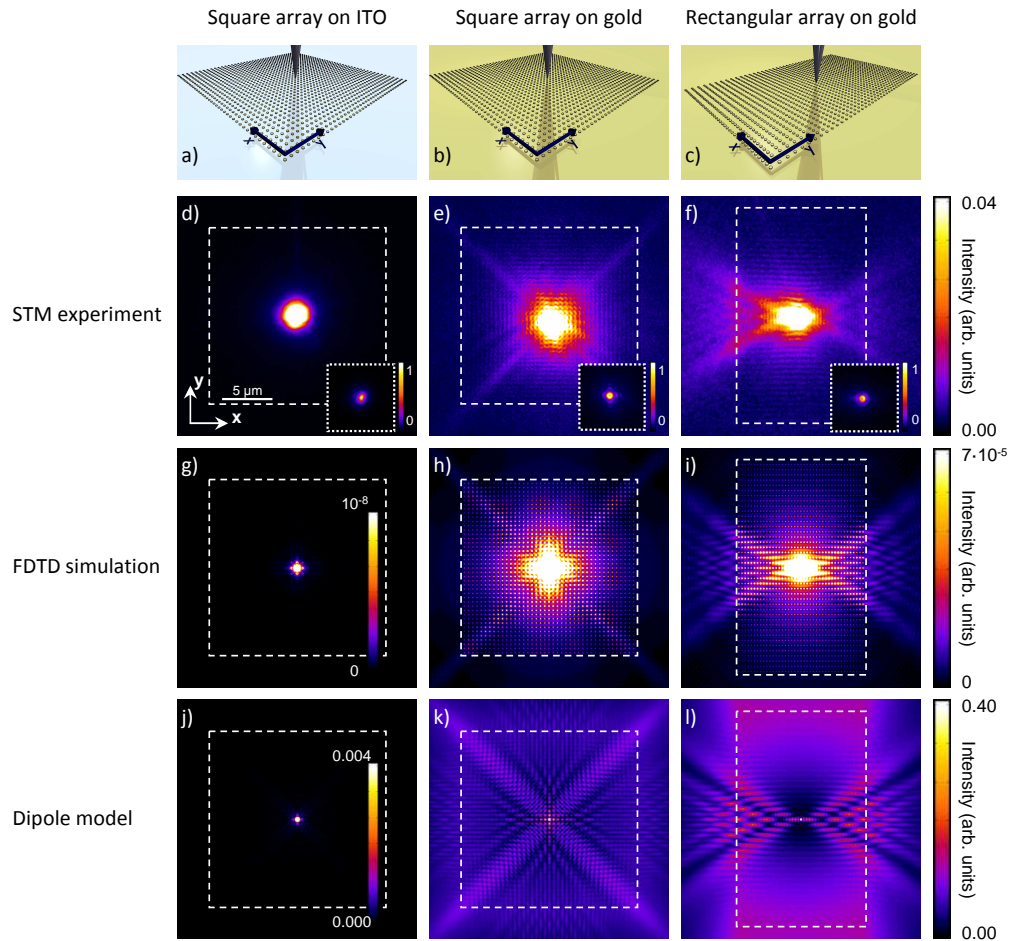


Fig. 2. Electrical excitation of plasmonic-crystal-gold-NP arrays: the effect of the substrate and array geometry. In this figure, the left and middle columns are the results for a square array on an ITO or 50-nm gold film respectively (unit cell $450 \times 450 \text{ nm}^2$). The right-hand column shows the results for a rectangular array with a $330 \times 550 \text{ nm}^2$ unit cell on a 50-nm gold film. [(a) to (c)] Schematics of the arrays indicating the STM tip excitation position on the sample. [(d) to (f)] Experimental real-space (far-field) microscopy images recorded upon electrical excitation of the array with the STM. The STM tip is located on a particle in the center of the array. All images are in false color and saturated (see color scale on the right, 1 in arbitrary units corresponds to the signal maximum intensity). The white dashed lines delimit the array in each image. Inset: unsaturated central areas of the images showing the lateral size of intensity peak at the tip location. [(g) to (l)] Theoretical squared electric field modulus in the near field above the array, obtained [(g) to (i)] through FDTD calculations where a vertical electric dipole is considered at the array center, and [(j) to (l)] using a simple model where both the excitation source and the scattering at the gold NPs are modeled as electric dipoles located on the NPs. In both approaches, the presence of the tip is ignored.

3.1. Substrate effects: the importance of surface waves

Comparing Figs. 2(d) and 2(e) clearly shows the crucial effect of the layer supporting the gold NP arrays (either ITO or gold). The emission of light is intense at the tip location as seen in the insets (unsaturated scale) of all three experimental real-space images [Figs. 2(d) to 2(f)]. This is the result of the radiative decay of the localized surface plasmon (LSP) of the gold NP below the STM tip. Yet saturating the intensity scale reveals the following: for the particle array on an ITO substrate, the excitation remains localized, but for an array on a gold film, there is an important *delocalized* contribution to the light emission [Figs. 2(e) and 2(f)]. This delocalized contribution is due to the SPP modes of the substrate excited by the particle LSP [39]. Thus we determine that the initial electrical excitation is mediated by the SPPs that propagate away from the gold NP under the tip and scatter on the other gold NPs, as revealed by the SPP leakage radiation collected in the substrate. In this way, then, the LSP coupling to surface waves greatly increases the reach of the primary excitation. On the other hand, a 100-nm layer of ITO on glass is too thin to support waveguide modes within the investigated energy range. Approximating the LSP mode as a dipole, the far-field radiation intensity decays as one over the square of the distance, faster than that for a circular outgoing surface plasmon wave ($I_{SPP} \propto \frac{1}{r}$). Consequently, the spatial distribution of the light in Fig. 2(d) is insensitive to the presence of the surrounding gold NPs with the possible exception of the nearest neighbors. Figures 2(g) to 2(l) show that the FDTD calculations and the simple dipole model confirm these experimental observations.

3.2. The effect of the array and of the array geometry: directional SPP emission

In order to clearly demonstrate the effect of the array on the SPP emission, Fig. 3 compares what is obtained for the electrical excitation of a thin gold film on glass [no NPs, Fig. 3(a)] to what is obtained for the electrical excitation of a square NP array on gold [Fig. 3(b)]. A distinctive difference is apparent: in the case of the array, four distinct preferential SPP propagation directions are seen. This difference is emphasized in Fig. 3(c) which is the intensity ratio of the normalized images of Figs. 3(a) and 3(b). A factor of ≈ 1.5 increase in the intensity is observed in four particular directions thanks to the presence of the array.

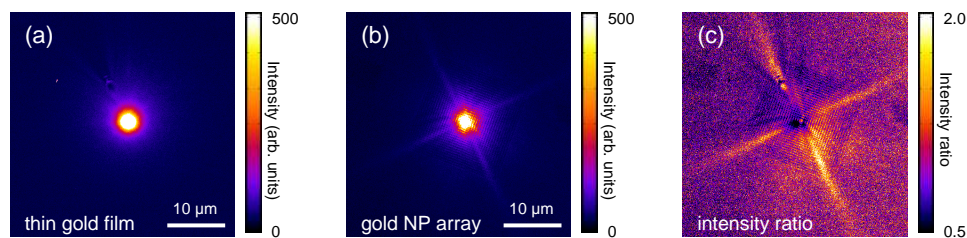


Fig. 3. Effect of the NP array on the SPP emission. (a) The electrical excitation of surface plasmons on a thin (50 nm) gold film on glass (no NPs). The leakage radiation detected beneath the substrate is isotropic, no preferred propagation directions for the SPPs are observed. (b) The electrical excitation of surface plasmons on a gold NP square array on a 50-nm thick gold film (unit cell $450 \times 450 \text{ nm}^2$). The leakage radiation signal shows four preferred SPP propagation directions. (c) Intensity ratio obtained when the data of part (b) is divided by the data of part (a). A factor of ≈ 1.5 increase in the intensity for particular directions is clearly seen when the array is present. In order to obtain part (c) of this figure, the data of parts (a) and (b) are first normalized with respect to the maximum intensity of the respective images.

Looking closely at Figs. 2(e) and 2(f) reveals that there are not only four distinct preferential SPP propagation directions for the square array, but also for the rectangular particle array on gold. The preferred SPP propagation directions are oriented along the diagonals of the square

array. The resulting SPP beams remain visible even beyond the array boundaries, i.e., on the unstructured gold film and the beams' full angular width at half intensity maximum (FWHM) is about 8° (i.e., the in-plane divergence is $\pm 4^\circ$ with respect to the mean propagation direction). On the rectangular array, four preferential SPP propagation directions are also clearly seen. They are oriented at an angle of about 30° with respect to the short axis of the rectangular array (FWHM $\approx 12^\circ$). Remarkably, both the FDTD calculations [Figs. 2(h) and 2(i)] and the simple dipole model [Figs. 2(k) and 2(l)] agree well with the directionality seen in the experimental real-space images.

Dark and bright fringes may be seen between the SPP beams identified in Figs. 2(e) and 2(f). The orientation of these fringes depends on their location in the image, but in each case they are parallel to one of the two array axes. The fringe period is equal to the pitch of the perpendicular array axis, i.e., the pitch of the axis to which the fringes are orthogonal (450 nm for the square array and 330/550 nm along the x/y axis of the rectangular array). Thus, since the fringes seem to coincide with the locations of the NP lines and rows, one might ascribe these fringes to the out-of-plane scattering of SPPs on the NPs; however, close to the source, the fringes bend visibly, whereas the NP lines and rows are straight. This suggests that the observed fringes are the result of interference in the near-field between the initial and in-plane scattered SPPs [40]. This near-field phenomenon is visible in real-space images since SPP leakage radiation mirrors the electric near field above the air-gold interface [41, 42].

The FDTD calculations in Figs. 2(h) and 2(i) are the result of a full electromagnetic modeling of the problem which includes all SPP scattering processes (i.e., both single and multiple in-plane SPP scattering off the NPs). Conversely, in the simple dipole model [Figs. 2(k) and 2(l)], the scattered emission from the NPs only depends on the scatterer's distance from the source. Nevertheless, both theoretical approaches reproduce well the preferential SPP propagation directions, including the differences between the square and rectangular arrays, and the additional fringe patterns that are observed in experiments.

3.3. The effect of the source location

In Sections 3.1 and 3.2, we specifically consider the case where the STM inelastic tunnel current electrically excites the *center* of the gold NP array. In this section, we investigate the effect of changing the local excitation source location. Figure 4 shows the real-space images recorded when the STM excitation is located at three particular positions on the square array: in the center, in the middle of a side, and at a corner. Bright-field transmission images [see Figs. 4(a) to 4(c)] show the position of the tip just before STM excitation: the center of the array in (a), the middle of the right side in (b) and the top right corner in (c). These bright-field images show the same area as the real-space images in Figs. 4(d) to 4(f) acquired via STM excitation.

Figures 4(d) to 4(f) show how the real-space images vary as a function of the tip excitation position. Figure 4(d) provides a more extended, unrotated view of the data already shown in Fig. 2(e), where the excitation source is in the center of a square array. Directional SPP emission along the diagonals of the square array is seen and the SPP beams continue far beyond the array boundaries (up to $25 \mu\text{m}$ away from the array corner). This effect is confirmed by the quantitative analysis of the angular distribution of the emitted SPP beams as shown in Fig. 5(a). In Fig. 5(a), the intensity from the real-space image is radially integrated to show the in-plane angular distribution of the emitted SPPs propagating away from the source, both *within* (black curve) and *outside* (red curve) the NP array area. The polar plots in Fig. 5(a) clearly show the four intensity peaks in the direction of the array diagonals [see also Fig. 5(d) for a schematic representation] as well as an isotropic background. We find that the SPP beams have a FWHM of 8° to 10° (once the isotropic background is subtracted) and the peak-to-background intensity ratio is about 2.

When the excitation point is located on the *side* of the array [see Fig. 4(e)], only *half* of the

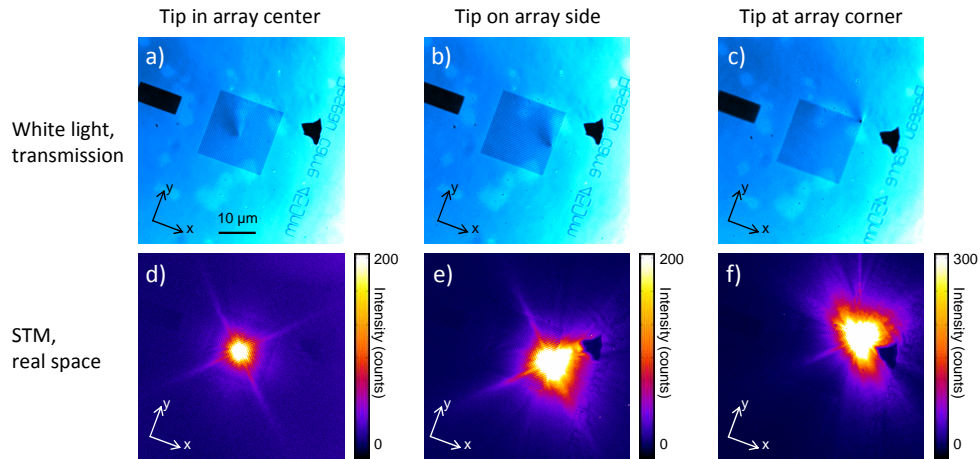


Fig. 4. The effect of excitation position. [(a) to (c)] Bright-field optical microscopy images measured upon white-light illumination of the sample (in transmission) with the STM tip present. The shadow of the tip end reveals its lateral position: in the center of the array in panel (a), in the middle of the right edge in panel (b) and at the top right corner of the array in panel (c). [(d) to (f)] Real space images acquired when the excitation position is (d) in the center, (e) on the side and (f) at the corner of the array. In this figure, all the data has been obtained on a square array of $450 \times 450 \text{ nm}^2$ unit cell on a 50-nm gold film (the array consists of 40×40 gold NPs). Images in panels (d) to (f) are in false color and saturated (intensity is given in photon counts). Exposure times range from 600 to 1800 s. STM bias is 2.8 V and the tunnel current setpoint is in the 0.1 – 6 nA range. The real space axes are defined with respect to the array axes.

SPP wavefront emitted from the source propagates through the array (i.e., the part corresponding to wavevectors with $k_x < 0$), while the other half propagates on the unstructured gold film (i.e., the part with $k_x > 0$). SPP beams with the same angular FWHM as above exist along the two diagonal directions for the part propagating *through* the array. Interestingly, the part of the wavefront that does *not* propagate through the array nevertheless also leads to SPP beams, but of much broader angular divergence [the FWHM is about 20° instead of 8° , see Figs. 5(b) and 5(e)]. When the local excitation position is located at the *corner* of the array [see Fig. 4(f) and Figs. 5(c) and 5(f)], a narrow (yet weaker) SPP beam starting at this corner and continuing diagonally through the array is created. As well, broader SPP beams are seen in the three other diagonal directions, similar to the case where the excitation is on the side of the array.

3.4. Simple model of SPP beam formation

Here we explain the SPP beaming effect seen in Fig. 4 in terms of the Bragg diffraction of the SPP wave from the 2D plasmonic crystal lattice (this is what we call the *simple wavevector model*). We consider the case where the excitation point is located in the center of the lattice [Fig. 4(d)]. The well-known Laue condition for diffraction of a wave by a regular lattice is [43]

$$\Delta \mathbf{k} = \mathbf{G} \quad (1)$$

In our case \mathbf{G} is a reciprocal lattice vector of the square 2D lattice and $\Delta \mathbf{k}$ is equal to $\mathbf{k}'_{\text{SPP}} - \mathbf{k}_{\text{SPP}}$ for the *in plane* scattering of SPPs into SPPs. \mathbf{k}_{SPP} and \mathbf{k}'_{SPP} are the initial and diffracted surface plasmon wavevectors respectively. Since the scattering is elastic, the magnitudes k_{SPP} and k'_{SPP} are equal, but their directions are different.

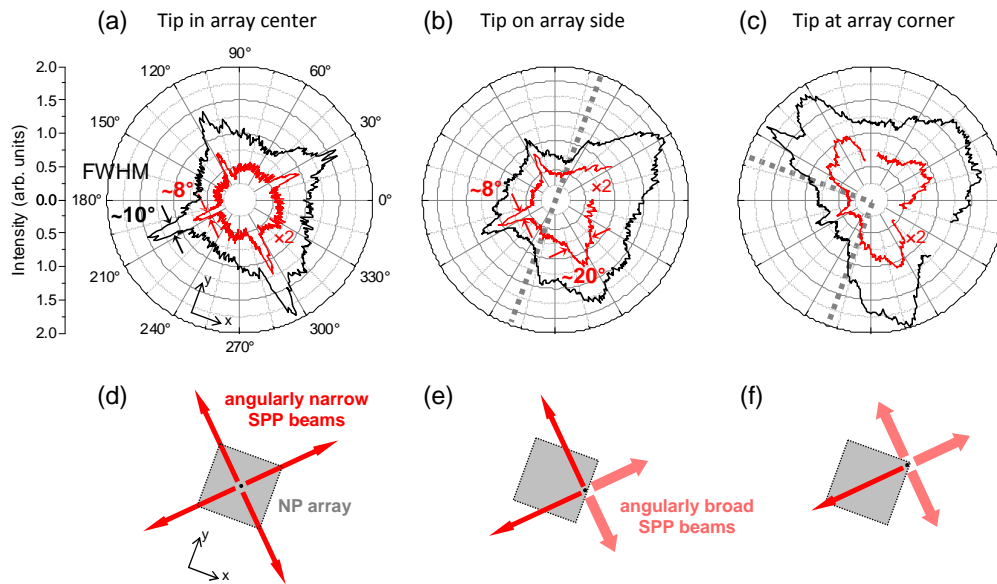


Fig. 5. In-plane angular distribution of the emitted SPP beams. [(a) to (c)] Polar plots obtained from the analysis of the real-space images shown in Figs. 4(d) to 4(f), respectively, and [(d) to (f)] schematics showing the preferential SPP propagation directions. In (a) to (c), we use a polar coordinate system where ρ is the lateral distance from the tip apex and ϕ is the polar angle in the surface plane. In each graph, the two plots correspond to the radially-integrated intensity over two different ranges of ρ , i.e., from $10\ \mu\text{m}$ to $15\ \mu\text{m}$ (black curve) and from $26\ \mu\text{m}$ to $31\ \mu\text{m}$ (red curve). In (a), these ranges of ρ correspond to (i) an area within the NP array (but far enough from the source to solely detect propagating SPPs) and (ii) an area just outside the NP array, respectively. The numbers on the graph are the full angular width at half maxima (FWHM) of the intensity peaks after the isotropic background is subtracted. Dashed lines in (b) and (c) indicate the directions of the array edges. In (d) to (f), thin and thick arrows indicate that angularly narrow (FWHM = 8° to 10°) and broad (FWHM $\approx 20^\circ$) SPP beams are observed in these directions, respectively.

Figure 6(a) is a schematic representation of the Fourier plane [see experimental Fourier-space image in Fig. 7(a)], where the two primary axis vectors of the square array reciprocal lattice, \mathbf{K}_a and \mathbf{K}_b , are drawn. In order to find the diffracted SPP wavevectors which satisfy Equation 1, we draw dashed circles of radius k_{SPP} centered on $\pm\mathbf{K}_a$ and $\pm\mathbf{K}_b$ [i.e., on the reciprocal lattice points $(\pm 1, 0)$ and $(0, \pm 1)$]. Drawing the vector from the reciprocal lattice point where the dashed circles cross the bright SPP ring of the experimental data gives us the scattered SPP wavevector for in-plane SPP-to-SPP scattering. Repositioning this vector \mathbf{k}'_{SPP} to start at $k = 0$ (i.e., the center of Fourier space) we see that these diffracted SPP waves are indeed emitted along the lattice diagonals as observed experimentally. The above discussion is valid for a plane wave; yet, the *cylindrical*, out-going, SPP wave that is emitted from the tip location in our case may be expressed as an infinite sum of SPP plane waves [44]. Note that the fact that the propagation directions correspond to the lattice diagonals is not a fundamental property of all square lattices but occurs when the SPP wavelength $\lambda_{SPP} = \frac{2\pi}{k_{SPP}}$ equals $\sqrt{2}$ times the array pitch, which is approximately the case here (the dashed circles in Fig. 6 are drawn for k_{SPP} corresponding to $\lambda_0 = 700\ \text{nm}$). This value was chosen since the broad spectrum that is measured experimentally is roughly centered at $\lambda_0 = 700\ \text{nm}$ (FWHM about $200\ \text{nm}$). The implications of a broadband source are discussed below. This leads to the dashed circles almost touching in Fig. 6(a) and four (instead of eight) beaming directions.

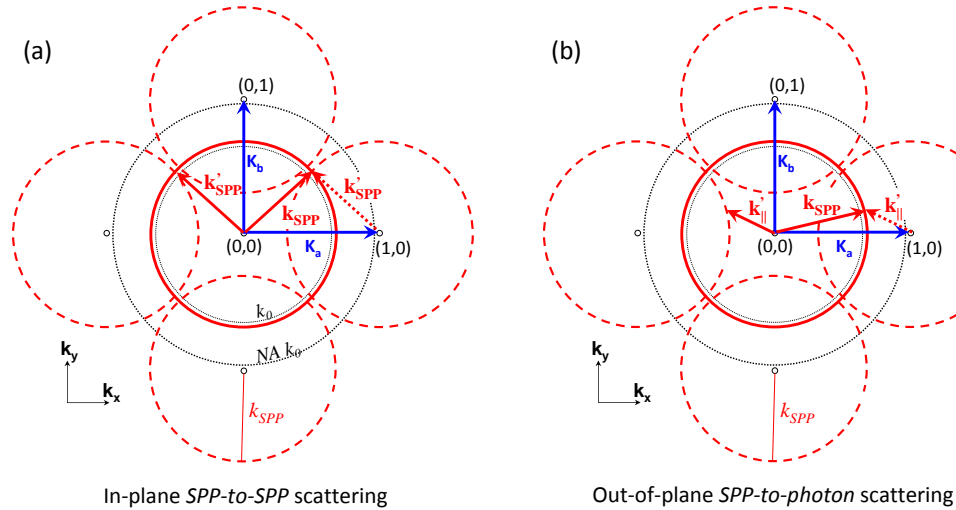


Fig. 6. Simple model explaining the directional propagation of locally-excited SPPs on a square nanoparticle array. (a) Diagram of the k_x - k_y Fourier plane for in-plane SPP-to-SPP scattering via the 2D lattice. The red circle centered on the Miller index (0,0) represents the SPP leakage radiation angle ($k_{||} = k_{SPP} \approx 1.037k_0$ at $\lambda_0 = 700$ nm). The black circle of smaller radius corresponds to the critical angle of the air-glass interface ($k_{||} = k_0$). The black circle of larger radius corresponds to the microscope objective numerical aperture ($k_{||} = NAk_0$ where $NA = 1.49$). \mathbf{K}_a and \mathbf{K}_b are the Bragg vectors of the square array, whose moduli in normalized Fourier coordinates are $\frac{K_a}{k_0} = \frac{K_b}{k_0} = \frac{\lambda_0}{a}$ where a is the array pitch ($a = 450$ nm). The dashed red circles have a radius k_{SPP} and are centered on the reciprocal lattice points $(\pm 1,0)$ and $(0,\pm 1)$. In (a), the Laue condition for a particular initial \mathbf{k}_{SPP} , with $\mathbf{G} = -\mathbf{K}_a$ is drawn, yielding \mathbf{k}'_{SPP} along the diagonal of the array. (b) Diagram of the k_x - k_y Fourier plane for out-of-plane SPP-to-photon scattering via the 2D lattice. $\mathbf{k}'_{||}$ is the in-plane component of the emitted photon.

As seen above, only SPPs traveling along the square array diagonals may be diffracted by the array into another diagonal, *in-plane* propagation direction. Thus SPPs with non-diagonal wavevectors may be transmitted or scattered *out of plane* into light (i.e., $\mathbf{k}'_{||} - \mathbf{k}_{SPP} = \mathbf{G}$ with $\mathbf{k}'_{||}$ the in-plane component of the emitted photon). This is shown schematically in Fig. 6(b). Due to this scattering into light for the other directions, the SPPs travel furthest along the diagonals: this is the explanation for the formation of the observed SPP beams.

Similar reasoning may be followed to explain the beaming effect observed in the case of the *rectangular* array [in Fig. 2(f)]. Here, the condition for in-plane (SPP-to-SPP) scattering through first-order diffraction into four (and not eight) preferred directions is $\lambda_{SPP} = \frac{2ab}{\sqrt{a^2+b^2}}$ where a and b are the array periods along x and y axes, respectively. For right-angled arrays, this configuration yields SPP beaming in directions that are off the x axis by an angle $\alpha = \arctan \frac{K_b}{K_a} = \arctan \frac{a}{b}$. Given $a = 330$ nm and $b = 550$ nm, one finds $\alpha \approx 31^\circ$, which is in good agreement with our experimental observations. Note that by construction in Fourier space, SPP beaming occurs along the $(\pm \mathbf{K}_a \pm \mathbf{K}_b)$ directions, which differ from the diagonals of the array unit cell in real space [i.e., the $(\pm \mathbf{a} \pm \mathbf{b})$ directions], except in the case of a square array (where $a = b$).

Another feature of the experimental data may be explained using the interpretation presented here. From the unsaturated Fourier space image in Fig. 7(b) obtained when the excitation is in the center of the array, we see that the intensity is maximum along the SPP ring in the preferential directions identified above as would be expected. Looking carefully at the same data but with a

saturated color scale in Fig. 7(a), we see V-shaped patterns at high k values in the directions corresponding to the diagonals of the array. As mentioned above, besides the special directions where SPPs may be reflected into SPPs, the SPPs propagating in other directions may be scattered into photons with $\mathbf{k}'_{\parallel} - \mathbf{k}_{\text{SPP}} = \mathbf{G}$. If $\frac{k'_{\parallel}}{k_0} < NA$ with NA the numerical aperture of the objective, the photons emitted in the glass substrate will be collected. Thus we expect to see the signature of these photons following the dashed white lines in the region of Fourier space where $\frac{k'_{\parallel}}{k_0} < NA$. This is most clearly seen in the regions where $1 < \frac{k'_{\parallel}}{k_0} < NA$, probably due to image contrast, thus yielding V-shaped features. The angular aperture of the V-shaped patterns is not perfectly reproduced using this simple model, since the source is considered monochromatic. The effect of the polychromatic nature of the source is discussed below.

3.5. The effect of a broadband excitation source

Light and SPPs generated from a tunnel junction are known to be spectrally broadband due to the nature of inelastic tunneling [30, 45]. In order to take into account the broadband distribution of the source in the numerical simulations and accurately reproduce the experimental observations, there are two possibilities: (i) the excitation in the junction may be modeled as a dipole oscillation of short duration (since a short pulse has a broad spectral distribution) or (ii) the results obtained for a series of monochromatic excitations may be summed incoherently using appropriate weighting factors (in a linear regime, both approaches are strictly equivalent). Here we use the second approach. Figures 7(e) to 7(g) are FDTD calculations of the Fourier plane obtained for a *monochromatic* source. They are obtained by taking the numerical Fourier transform of images similar to those shown in Fig. 2(h), (the complex electric field is Fourier transformed and its squared modulus is displayed). A weighted sum of this series is then used to obtain the equivalent of a *polychromatic* Fourier-space image in Figs. 7(c) and 7(d) (the signal above $k_{\parallel} = 1.49k_0$ is truncated in order to simulate the NA of the objective lens). This theoretical result is compared to the experimental Fourier-space image in Figs. 7(a) and 7(b). Images with both saturated and unsaturated intensity scales are shown so that the agreement between theory and experiment with regards to the intensity maxima along the SPP ring as well as the V-shaped features is apparent.

Since the monochromatic Fourier-space images [Figs. 7(e) to 7(g)] are images of k -space for specific free-space wavelengths or energies, the dispersion relation for SPPs propagating in the gold NP array may be determined from such calculations. We also clearly see in such images that SPP propagation in the NP array is anisotropic and thus different from the symmetric SPP propagation on a planar gold film. In particular, for certain wavelengths, directions where propagation is forbidden may be identified. This information is central for the characterization of the system in view of its integration in a device, if, for example, this system is to be used as an electrical nanosource of propagating waves.

The monochromatic calculations shown in Figs. 7(e) to 7(g) reveal other interesting features in the four diagonal directions identified in Fig. 4. Interference between the unscattered/initial and scattered/reflected SPP waves locally modifies the shape and intensity of the SPP ring at these four particular points. This phenomenon has already been reported in the case of laser-excited 2D sinusoidal gratings on gold, and was described as gap openings in the SPP dispersion due to the coupling of the array diffraction orders [27, 28]. The unusual form of the SPP ring near these points (similar to an anti-crossing) has been used for SPP beam steering [27], negative refraction [27] and self-collimation [28]. The resulting modification of the SPP propagation properties are explained in terms of propagating plasmonic Bloch waves. This formalism is equivalent to the simplified model that we use in Fig. 6. Importantly, the effects described in Refs. [27, 28] are highly sensitive to the oscillation frequency. In our case, due to spectral averaging, gap openings may not be distinguished in both the experimental and theoretical results of Figs. 7(a) to 7(d); instead, the Fourier images differ from those of an unstructured gold film by

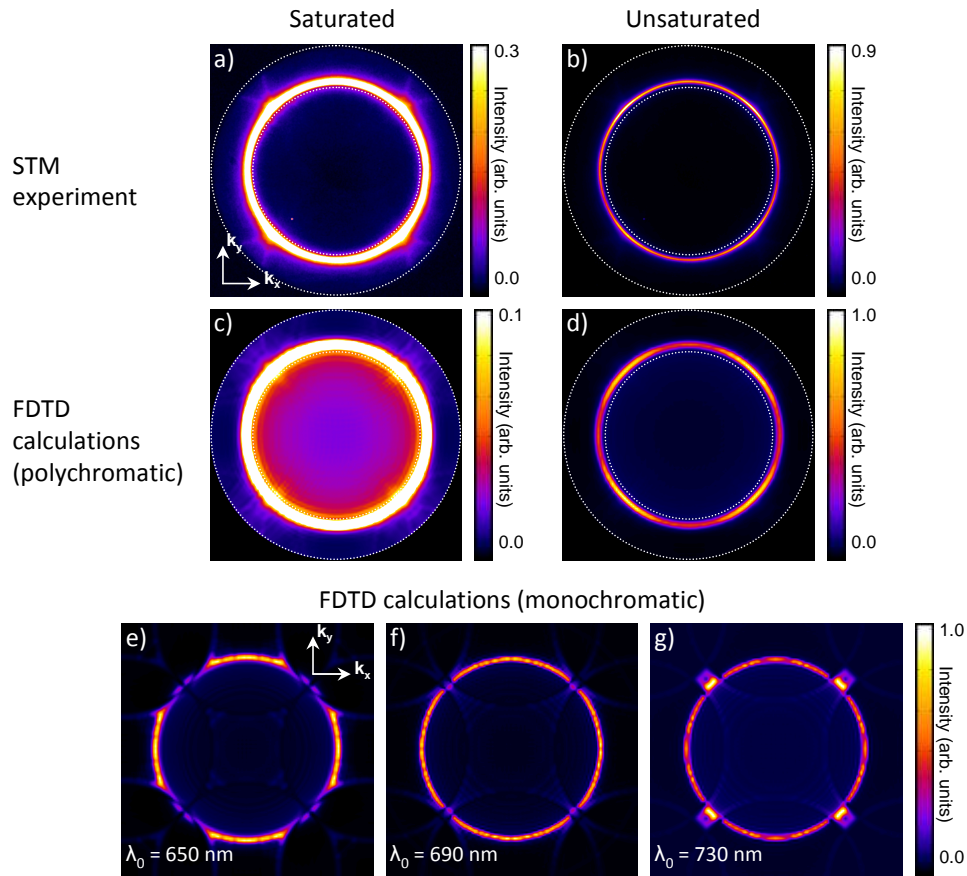


Fig. 7. The effect of the broadband spectrum of the excitation source. [(a) and (b)] Experimental and [(c) and (d)] theoretical Fourier-space images of the light emitted from the STM excitation of a square array on a gold film. The STM tip is centered on a gold NP in the array center. Panels (a),(c) show the same data as panels (b), (d), but with a saturated color scale so that the details of the images may be seen. The theoretical images shown in panels (c) and (d) are obtained from the weighted average of the results from monochromatic FDTD calculations at different energies (see Sec. 2.3); the weighting factors are determined from the experimental emission spectrum of the excitation source. [(e) to (g)] Three images taken from the series of monochromatic FDTD calculations used to produce the polychromatic result shown in panels (c) and (d). The theoretical Fourier-space images are obtained by Fourier transforming the calculated electric field above the gold NP array, taking the squared modulus of the result and finally truncating it at the angular acceptance limit of the objective lens. Panels (e) to (g), however, show the images before truncation. The array unit cell is $450 \times 450 \text{ nm}^2$ and the gold film thickness is 50 nm.

the increased intensity of the SPP ring in the four directions where SPP beaming occurs.

As well, it may be seen from the monochromatic FDTD calculations that the SPP ring is only bright in the beaming directions for the long wavelength calculation [$\lambda_0 = 730$ nm, in Fig. 7(g)], whereas the SPP ring is comparatively dark in the beaming directions for shorter wavelengths [$\lambda_0 = 650$ nm and 690 nm, in Figs. 7(e) and 7(f), respectively]. From these observations, we infer that SPP beaming along the array diagonals essentially occurs at SPP wavelengths that are longer than the diagonal of the array cell, most probably because the incident and scattered SPP waves only interfere constructively in this case. Given that the excitation source has a broad power spectrum centered at $\lambda_0 \approx 700$ nm, we expect that a shorter array period would yield on average a stronger SPP beaming effect since the incident and scattered SPP waves would interfere constructively within a larger domain of the emission spectrum.

3.6. Final discussion on the efficiency to generate SPP beams

The gold NP array may be regarded as a functional device with the ability to generate directional SPP beams. A rough estimation of the efficiency (the number of plasmons per electron) of this device may be deduced as follows. According to Johansson [30], “at most a few percent of all the electrons undergo some inelastic process while in the gap between the tip and sample.” Bigourdan et al. [46] have calculated the efficiency of a “tungsten sphere-gold film” tunnel junction to produce SPPs on the gold film and they evaluate the ratio of the SPP power to the excitation source power to be between 10^{-4} and 10^{-3} . Therefore, we may estimate the total SPP excitation efficiency in our electrical excitation setup at 10^{-6} to 10^{-5} SPP/electron. It should be noted, however, that this efficiency is expected to increase by over 2 orders of magnitude through the use of nanoantennas [46].

As well, the intensity ratio of the final output directional SPP beams to the initially excited SPP may be evaluated from the data shown in Fig. 3. On an unstructured gold film, the intensity ratio between the SPPs at a distance d from the excitation source to the initially excited SPPs is simply given by the expression for a cylindrical wave: $\frac{I(d)}{I(0)} = \frac{\exp(-2k''_{SPP}d)}{d}$, where k''_{SPP} is the imaginary part of the SPP wavevector. Fig. 3(c) shows that when using the square-lattice array, the SPP intensity in the diagonal directions is ≈ 1.5 times as high as that of the SPPs emitted in absence of the array, at the same distance from the excitation source. More importantly, the intensity ratio of the SPPs emitted in the diagonal directions to those emitted in other directions is equal to about 2.

4. Conclusion

We have investigated the optical response of gold NP arrays on gold and ITO to a local, electrical excitation based on the low-energy tunnel electrons from the tip of an STM. On ITO, this optical response is essentially *local*, due to the rapid spatial decay of the electric field from the source and the broadband spectrum of the IET-induced light. This is in contrast to the strong collective effects reported in the literature in the case of normal-incidence plane-wave optical excitation, where all NPs are coherently excited with the same intensity and the scattered radiation interferes *in the far field* on the detector [34, 35]. Conversely, a *delocalized* optical response to the electrical excitation is observed for gold NP arrays on a gold film, since the substrate supports surface waves. SPPs propagate away from the excitation source (on the air side of the gold film) and are scattered in-plane (into SPPs) and out-of-plane (into light) by the NP array. Interference *in the near field* between the emitted and in-plane scattered SPPs yields strong directional effects in SPP propagation, which are observed in the SPP leakage radiation pattern. We elucidate the occurrence of such SPP beaming using a simple model based on the scattering of SPPs by an array. As well, due to the broadband nature of the source, the gap openings that are expected in the SPP dispersion relation for these plasmonic systems are not experimentally observed, in agreement with polychromatic FDTD calculations. These observations provide new insight

into the future integration of plasmonic crystals with nanoelectronics where local, low-energy, electrical nanosources of SPPs are coupled to the extended modes of plasmonic crystals.

Funding

Région Ile-de-France, DIM Nano-K; LabEx NanoSaclay (ANR-10-LABX-0035-NanoSaclay).

Acknowledgments

The gold nanoparticle arrays were fabricated at the technological platform for nano and microfabrication *Planète* in Marseille. *Planète* is part of the Technological Center of the Région Provence-Alpes-Côtes-d'Azur. The authors acknowledge financial support by the Région Ile-de-France in the framework of DIM Nano-K and by "Investissements d'Avenir" LabEx NanoSaclay.